Research Article

NMR IN BIOMEDICINE

Received: 16 August 2011, Revised: 15 November 2011, Accepted: 29 November 2011, Published online in Wiley Online Library: 26 February 2012

(wileyonlinelibrary.com) DOI: 10.1002/nbm.2769

A novel method for simultaneous 3D B_1 and T_1 mapping: the method of slopes (MoS)

Sofia Chavez[a]* and Greg J. Stanisz[b]

A novel three-dimensional simultaneous B_1 and T_1 mapping method is introduced: the method of slopes (MoS). The linearity of the spoiled gradient recalled echo (SPGR) signal *vs* flip angle relation is exploited: B_1 mapping is achieved by a two-point extrapolation to signal null with a correction scheme while T_1 mapping uses the slopes of the SPGR signal *vs* flip angle curves near the origin and near the signal null. This new method improves upon the existing variable flip angle (VFA) T_1-mapping method in that (i) consistency between B_1 and T_1 maps is ensured (ii) the sampling scheme is T_1-independent (iii) the noise bias and singularity, associated with using a linear form for the SPGR signal equation, is eliminated by using the full equation. The method is shown to yield accurate and robust results *via* simulations. Initial estimates of B_1 and T_1 values are obtained from three data points *via* simple computations and straight line approximations. Initial estimates of B_1 values, for a range of values, are shown to be accurate due to the proposed B_1 correction scheme. The accuracy and robustness of T_1 values is achieved *via* a non-linear fitting algorithm which includes a fourth data point sampled at high SNR. The MoS was validated by comparing resulting B_1 and T_1 maps with those obtained using other standard methods. Finally, the ability to obtain brain B_1 and T_1 maps using the MoS was demonstrated by *in vivo* experiments. The MoS is expected to perform well on other motion-free anatomical regions as well. Copyright © 2012 John Wiley & Sons, Ltd.

Keywords: B_1 inhomogeneities; T_1 mapping; SPGR; flip angle; spoiled-gradient-echo

INTRODUCTION

Spatial quantification of the longitudinal relaxation time, T_1 mapping, is of great interest for many clinical MR applications because T_1 is known to be an important marker of varying pathological conditions such as cancer (1,2), multiple sclerosis (3,4) and arteriosclerosis (5). There is a high demand for efficient and accurate T_1 mapping methods that can be implemented at high spatial resolution, over large volumes of interest in a clinically reasonable time (scan time $<$ 20 min). An inversion-recovery (IR) remains the gold-standard for T_1 mapping but due to the requirement of a long repetition time, *TR*, this method is prohibitively time-consuming. Newer methods eliminate the long *TR* requirement by using transient to steady-state (SS) or SS signal dependencies: Look-Locker (LL) based techniques (6–8) and variable flip angle (VFA) methods (9–12), respectively. All methods sample the signal under varying conditions and then fit the result to an expected T_1-dependent signal model.

Although LL techniques do not require long *TR*, they are still time-consuming due to the many time points required. Therefore, LL techniques are usually implemented with fast readout acquisitions, such as echo-planar imaging (EPI) (7,8), which may introduce signal modulations, compromising the accuracy of the T_1 estimates. Although VFA T_1-mapping techniques (such as DESPOT1: driven equilibrium single-point observation T_1) are very time efficient, the result has been shown to be very sensitive to noise bias and the choice of flip angles used (9–11). Inconsistency in T_1 values reported in the literature may be a result of these biases. New techniques for T_1 mapping remains an active area of research (13,14). At high field strengths (≥3T), both types of techniques are prone to errors introduced by spatial inhomogeneities of the RF (radiofrequency) field called B_1. B_1 inhomogeneities can become a dominating factor in the systematic errors affecting T_1 estimates (12,14).

At high field strengths, B_1 inhomogeneities introduce spatial variations to the flip angle and thus signal. These inhomogeneities originate from two inherent sources: non-uniformity of the transmit field and the so-called dielectric effect which occurs when the dielectric constant of the imaged tissue causes the RF wavelength to approach the dimensions of the imaged object (2–20 cm @ 3T depending on the dielectric properties of the tissue (15)). Fast T_1 mapping techniques rely on an accurate assessment of the flip angle, thus this effect needs to be measured, and accounted for in the fitting algorithms, to ensure accuracy of the T_1 mapping techniques mentioned above. A linear relationship is expected to exist between the B_1 field strength and flip angle thus

* *Correspondence to: Dr. S. Chavez, Research Imaging Centre, Centre for Addiction and Mental Health, 250 College Street Toronto, ON, Canada M5T 1R8. E-mail: sofiachavez@camhpet.ca*

a *S. Chavez*
Research Imaging Centre, Centre for Addiction and Mental Health, Toronto, ON, Canada

b *G. J. Stanisz*
Department of Medical Biophysics, University of Toronto and Imaging Research, Sunnybrook Health Sciences Centre, Bayview, Toronto, ON, Canada

Abbreviations used: *α, flip angle; C_α, flip angle calibration factor; AFI, actual flip angle imaging; a.u., arbitrary units; DAM, double-angle method for flip angle mapping; DESPOT1, driven equilibrium single-point observation T_1 EPI, echo-planar; IR, inversion-recovery; LL, Look-Locker; MoS, method of slopes; NLLS, non-linear least squares; ROI, region of interest; SE, spin echo; SI, signal intensity; SNR, signal-to-noise ratio; SPGR, spoiled-gradient-recalled-echo; SS, steady-state; TI, inversion time; VFA, variable flip angle.*

the spatial quantification of this source of error is commonly referred to as B_1 mapping. Furthermore, it has been shown that the actual flip angle is linearly related to the nominal flip angle (that prescribed on the scanner) for a range of flip angles (12). Specifically, a B_1 map usually refers to a map of the calibration factor relating the actual flip angle to the nominal flip angle. Although the relationship between actual and nominal flip angles herein is assumed to be due to these inherent B_1 inhomogeneities, proper calibration of the transmit gain can also affect flip angle accuracy. This component is scanner/user dependent and for most scanners it can be expected to be automated and accurate. However, if present, such systematic errors are assumed to result in linear inaccuracies in the true flip angle as well.

Both LL and VFA T_1 mapping techniques require separate B_1 mapping to account for flip angle variations. Separating B_1 and T_1 mapping processes can be problematic because of the inconsistency in implementation: B_1 mapping is often implemented in two-dimensions (2D) due to time constraints while T_1 mapping usually requires three-dimensional (3D) acquisitions for accurate quantitative signal. Effects of the slice profile differences compromise the accuracy when a 2D B_1 mapping technique is used to correct a 3D T_1 mapping technique. This potential source of error in T_1 estimation is usually ignored, although it is mentioned in the literature (11).

Standard B_1 mapping techniques can be very time-consuming and there is still no gold standard. A common and simple method is the double-angle method (DAM) which requires the acquisition of two images with fully relaxed signal ($TR \geq 5\ T_1$) at two different flip angles. For practical purposes, time limitations require that the DAM be implemented with either fast imaging techniques (16), which may add artifacts, or special pulses (17), which are not readily available. Other methods for B_1 mapping include the phase-sensitive method (18) and more recently, actual flip angle imaging (AFI) (19) and the method based on the Bloch-Siegert shift (20). However, these methods are not readily available since they require specially designed pulse sequences. A simple and accurate B_1 mapping method that makes use of the signal null point has already been proposed by Dowell and Tofts (21). This method is rarely used, perhaps due to the high flip angle requirement ($>180°$) which is difficult to achieve on a typical scanner. Recent studies have demonstrated that T_1 mapping is very sensitive to the method of B_1 mapping chosen for flip angle correction due to the variation in B_1 mapping results (22). This emphasizes the importance of a consistent, accurate, simultaneous B_1 and T_1 mapping method.

Although a few methods have been proposed to simultaneously yield B_1 and T_1 maps (23–25), they are not easy to implement as they require additional acquisitions (23,24) or look-up tables (25) and elaborate fitting algorithms to de-couple the signal dependence on the various parameters. A simple, readily available simultaneous B_1 and T_1 mapping method is therefore of great interest and the aim of this work.

The new technique, proposed in this paper, relies on the expression for the spoiled-gradient-recalled-echo (SPGR) signal as a function of flip angle and T_1. It makes use of a straight line extrapolation to determine the signal null point as proposed in Ref. 21 for B_1 mapping, but an improved implementation with fewer samples (2 instead of 3) and for smaller flip angles ($<180°$) is proposed. It also exploits the linearity of the signal *vs* flip angle curves to obtain T_1 maps. This 3D technique can be applied in a practical time by reducing data redundancy as data used for B_1 mapping is also used for T_1 mapping.

THEORY

The signal intensity (*SI*) resulting from an SPGR acquisition can be described as:

$$SI = S_0 \sin(\alpha)\frac{1-E_1}{1-\cos(\alpha)E_1} \quad [1]$$

where S_0 represents the equilibrium signal and encompasses the effects of receiver coil sensitivity, proton density and T_2^* attenuation while $E_1 = \exp(-TR/T_1)$. The nominal flip angle, α_{nom}, and the true flip angle, α, are related by:

$$\alpha = C_\alpha \cdot \alpha_{nom} \quad [2]$$

where C_α is a spatially varying calibration factor that is independent of α_{nom} (12).

There is high coupling between the three independent parameters: C_α, S_0 and T_1, in Equation [1], making their simultaneous estimation an ill-posed problem. This has been noted by others (23,24) who justify the inclusion of additional acquisitions. The method presented in this paper exploits the linearity of the SPGR signal *vs* flip angle curve, at low and high flip angles, to decouple and uniquely determine C_α, S_0 and T_1.

SPGR *vs* flip angle curves

Figure 1a shows curves representing the SPGR signal as a function α_{nom} described by Equation [1] for the fixed values: $S_0 = 100$ (in a.u. = arbitrary units) and $C_\alpha = 1$. S_0 simply scales the signal, resulting in a vertical stretching/contracting of the curve while C_α scales the true flip angle, causing a horizontal stretching/ contracting of the curves. For a constant *TR*, the curve warps downwards and towards the left with increasing T_1 (as the Ernst angle, α_{Ernst}, shifts to smaller values: $\alpha_{Ernst} = \cos^{-1}(E_1)/C_\alpha$).

These curves have three useful features. First, note that C_α is uniquely defined at the signal null point, when the SPGR curve first crosses the *x*-axis for values of $\alpha_{nom} > 0°$: $SI(\alpha_{nom} = \alpha_{null}) = 0$. This null point occurs when $\alpha = 180°$ hence C_α can be derived as: $C_\alpha = 180°/\alpha_{null}$ (21). Second, for flip angles near the origin and near the null point, the signal dependence on flip angle is approximately linear. Third, Fig. 1 shows that the curves fan out and then converge at the signal null whilst overlapping for low flip angles. Thus, the signal contrast for different T_1 values is higher just after the Ernst angle, and very low at low flip angles.

Derivative of the SPGR *vs* flip angle curves

Consider the derivative of Equation [1] with respect to true flip angle:

$$SI' = \frac{\partial SI}{\partial \alpha} = \frac{S_0 C_\alpha (1-E_1)}{(1-\cos(C_\alpha \alpha_{nom})\cdot E_1)^2}(\cos(C_\alpha \alpha_{nom}) - E_1) \quad [3]$$

Figure 1b shows plots of SI' as a function of α ($C_\alpha = 1$), for several TR/T_1 values, in the high flip angle region. These curves suggest that the straight line extrapolation to the signal null point is justified under two conditions: TR/T_1 is small ($<1/5$) and the signal is sampled in the linear region which, based on these simulations, is assumed to hold for $\alpha \geq 150°$. There is a practical limitation for how small TR/T_1 should be since as TR/T_1 decreases, the derivative approaches zero and the extrapolation to the null point could be compromised, depending on the signal-to-noise ratio (SNR).

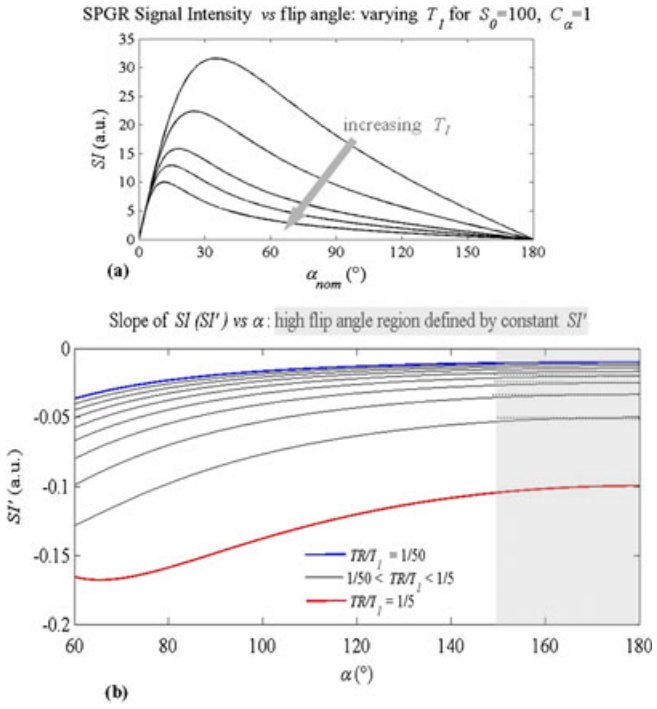

Figure 1. Plots of SPGR Signal Intensity (*SI*) and its derivative (*SI'*) in *arbitrary units*, a.u., as a function of nominal flip angle, α_{nom}. (a) $C_\alpha = 1$, $S_0 = 100$ and TR/T_1 is varied: as TR/T_1 decreases or T_1 increases, curves shift down and towards the left (Ernst angle moves to smaller values of α_{nom}). (b) Derivative of SPGR Signal (*SI'*) as a function of true flip angle (α). The high flip angle region is defined as being the region with constant *SI'* and thus an extrapolation to signal null is justified. The curves correspond to varying T_1 values (with fixed *TR*) showing that the constant *SI'* region is larger for greater T_1 values. Based on these plots, the high flip angle region is chosen to be $\alpha \geq 150^\circ$(shaded region).

To approximate the slope near the origin and near the null point, two limits are taken: $SI'_0 = lim_{\alpha \to 0^\circ}$ and $SI'_{null} = lim_{\alpha \to 180^\circ}$ respectively. Computing the two limits using Equation [3] yields:

$$\left.\begin{aligned} SI'_0 &= S_0 C_\alpha \\ SI'_{null} &= \frac{-S_0 C_\alpha (1 - E_1)}{(1 + E_1)} \end{aligned}\right\} \quad [4]$$

Hence SI'_0 and SI'_{null} depend linearly on C_α and S_0 whilst SI'_0 does not depend on E_1. A ratio of the slopes thus uniquely defines E_1 (i.e. T_1) as follows:

$$\begin{aligned} SI'_{null}/SI'_0 &= -(1 - E_1)/(1 + E_1) \\ E_1 &= -\frac{\left[(SI'_{null}/SI'_0) + 1\right]}{\left[(SI'_{null}/SI'_0) - 1\right]} \end{aligned} \quad [5]$$

Proposed Method of Slopes (MoS)

The proposed method, herein called MoS (Method of Slopes), aims to provide simultaneous B_1 and T_1 maps as follows: (i) the signal *vs* nominal flip angle curve is sampled at high flip angles and a straight line is fit to the data to extrapolate to the signal null point (when $\alpha = 180^\circ$), yielding the B_1 map (ii) this straight line also yields the slope value: SI'_{null}, (iii) a straight line is then approximated between the low flip angle data and the origin yielding an estimate for SI'_0, and (iv) the ratio of these slopes is used to calculate the T_1 map according to Equation [5] where $T_1 = -TR/ln(E_1)$.

Although the B_1 mapping part of this new method is conceptually the same as that presented previously (21), a slightly simpler approach is taken: the sampling scheme was chosen such that all magnitude signal values are expected to be true positive signal values. This is accomplished by limiting the sampling to flip angles smaller than α_{null}. Although the exact value of α_{null} is not known *a priori*, the smallest possible value for α_{null} can be estimated for a given transmit coil and object being imaged. For brain imaging (with either the 8-channel or transmit/receive head coil) α_{null} is not expected to be less than 150° at any voxel.

The accuracy of the proposed method depends on the accuracy of the straight line approximations. Figure 1 suggests that Equation [5] may be a good approximation for straight line fits over a range of flip angle values near 0° and α_{null}. Although high flip angle data must be sampled in a region near α_{null}, this value is not known *a priori* and furthermore, α_{null} is expected to vary spatially due to significant B_1 variations. Also, one must consider the number of data points required to produce reliable and accurate approximations of the slopes. These concerns will be addressed in this section.

In theory, two points are sufficient to evaluate the slope of any straight line. Moreover, minimizing the number of sampling points increases efficiency. For the low flip angle straight line evaluation, the origin ($\alpha = 0^\circ$, $SI = 0$) can be used as one of the data points hence a single sample at low flip angle ($\alpha_{nom} = 1^\circ$) should be sufficient. Sampling the high flip angle range is more problematic due to the deviation from linearity depending on C_α as illustrated in Fig. 2. If the linear region near the null point is sampled for the curve with largest C_α (i.e. smallest $\alpha_{null} \sim 150^\circ$), the sampling scheme will not sample the linear region of curves with smaller C_α and larger α_{null}. In fact, the extrapolation to α_{null} for other curves leads to an underestimation of α_{null} which worsens as the value of α_{null} increases (arrows in Fig. 2). For accurate B_1 mapping, the challenge lies in the accurate determination

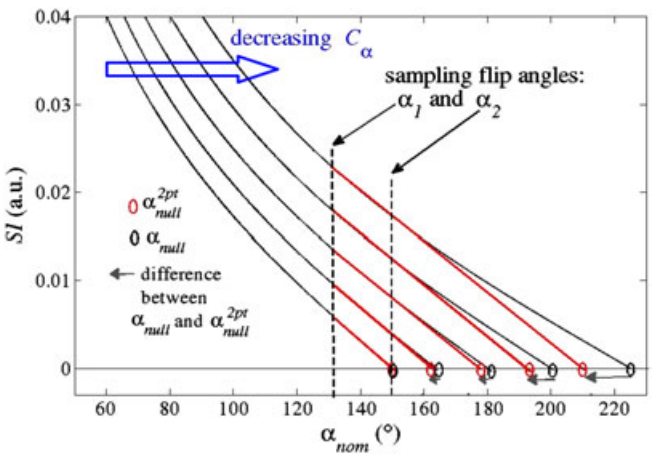

Figure 2. Zoom of SPGR signal intensity (SI) *vs* nominal flip angle (α_{nom}) curves in region of signal nulling. Curves have constant TR/T_1 and S_0 while C_α is varying from 1.2 to 0.8. The red lines indicate the 2 pt-extrapolation based on sampling the signal at 2 flip angles: α_1 and α_2. This plot shows that the 2 pt- extrapolated flip angle for signal null, α^{2pt}_{null}, *under*estimates α_{null} (i.e. C^{2pt}_α *over*estimates C_α), as indicated by the small arrows along the bottom axis. Furthermore, this underestimation increases as C_α decreases (from left to right).

of α_{null} even if the sampled flip angles are not within the linear region. This problem can be solved by introducing a C_α -correction scheme as follows.

We wish to determine α_{null} by extrapolating the data acquired at nominal flip angles: α_1 and α_2 (where $\alpha_1 < \alpha_2$). To do this effectively, we derive a function that relates the estimated flip angle for signal null: α_{null}^{2pt}, derived from the extrapolation of $SI(\alpha_1)$ and $SI(\alpha_2)$, to the true flip angle for signal null: α_{null} (see Appendix). We show that although this cannot be solved analytically, a smoothly varying function exists, relating α_{null}^{2pt} to α_{null} (Fig. A1). Furthermore, the relationship can be used to determine a correction scheme which maps the B_1 calibration factor determined from α_{null}^{2pt}, called C_α^{2pt}, to the true B_1 calibration factor C_α. Using Equation [A5] and expressing $C_\alpha^{2pt}\cdot\alpha_2$ as a function of $C_\alpha\cdot\alpha_2$ (where $C_\alpha^{2pt}\cdot\alpha_2 = 180^\circ/\left(\alpha_{null}^{2pt}/\alpha_2\right)$) gives:

$$C_\alpha^{2pt}\cdot\alpha_2 = 180^\circ\cdot\frac{A(C_\alpha\cdot f\cdot\alpha_2)\cdot B(C_\alpha\cdot\alpha_2) - A(C_\alpha\cdot\alpha_2)\cdot B(C_\alpha\cdot f\cdot\alpha_2)}{A(C_\alpha\cdot f\cdot\alpha_2)\cdot B(C_\alpha\cdot\alpha_2) - f\cdot A(C_\alpha\cdot\alpha_2)\cdot B(C_\alpha\cdot f\cdot\alpha_2)} \quad [6]$$

where $f = \alpha_1/\alpha_2$ and, to simplify the above expression, for a given angle ϕ, A and B are defined as: $A(\phi) = sin(\phi)$, $B(\phi) = (1\text{-}E_1\cdot cos(\phi))$. For a chosen value of f and E_1, Equation [6] can be used to plot points corresponding to $C_\alpha\cdot\alpha_2$ *vs* $C_\alpha^{2pt}\cdot\alpha_2$ which are then fit by a quadratic function. Figure 3 shows a plot of generated data points whereby Equation [6] has been evaluated for values of $C_\alpha\cdot\alpha_2 \le 180^\circ$ (since α_2 is chosen such that $\alpha_2 \le \alpha_{null}$ and $C_\alpha\cdot\alpha_{null} = 180^\circ$ by definition). For this example, $f = 130^\circ/150^\circ$ and $E_1 = 0.96$ were used since practical scanning values are: $TR = 40$ ms and an average T_1 of interest is $T_1 = 1000$ ms. As shown in the Appendix, the curves are not very sensitive to T_1 values (within the range: $1/50 < TR/T_1 < 1/5$), so an approximate value is sufficient. For this example, we get:

$$Y = -aX^2 + bX - c \quad [7]$$

where $Y = C_\alpha\cdot\alpha_2$, $X = C_\alpha^{2pt}\cdot\alpha_2$ and the fit parameters are $a = 0.00496$, $b = 2.72$ and $c = 150$. We can use this to write a more general form:

$$C_\alpha = -(a\cdot\alpha_2)\cdot\left(C_\alpha^{2pt}\right)^2 + b\cdot C_\alpha^{2pt} - c/\alpha_2 \quad [8]$$

where $a = 0.00496$, $b = 2.72$ and $c = 150$

Using Equation [8] to go from C_α^{2pt} to C_α gives the sought C_α-correction scheme as a function of α_2. This scheme allows for accurate estimates of C_α despite sampling the data away from the linear region.

Ultimately, C_α and SI'_0 can be used to derive S_0 according to Equation [4] or the ratio of slopes can be used to estimate T_1. As described thus far, the MoS assumes straight lines between two data points, thus no data fitting is required. However, T_1 accuracy is expected to be compromised due to the approximations involved and the fact that signal is sampled at low and high flip angles with relatively low SNR. The final step of the MoS therefore involves feeding these straight line initial estimates of T_1 and S_0 to a NLLS (non-linear least squares) fitting algorithm which aims to best fit the data to a curve predicted by Equation [1]. This fitting procedure is performed while including an additional data point sampled in the region of high SNR and where the signal dependence on T_1 is greatest. A good value for this was found to be $\alpha_{nom} = 40^\circ$.The steps for MoS are summarized in Fig.4.

Optimizing the MoS for scan time efficiency

Consider the limitations for accurate estimation of the sought parameters: B_1 and T_1, and the contribution of each of the four sampled data points to the results. In particular, note that the two data points at high flip angle values: $\alpha_{nom} = (130^\circ, 150^\circ)$ are essential for B_1 mapping while the small flip angle data point at $\alpha_{nom} = 1^\circ$determines S_0, given B_1. Although the slopes of these straight line fits are used as initial T_1 estimates, the data point at high signal, $\alpha_{nom} = 40^\circ$, is responsible for the final T_1 result given the high signal dependence on T_1 at this flip angle value. These considerations can be used to optimize the MoS for time

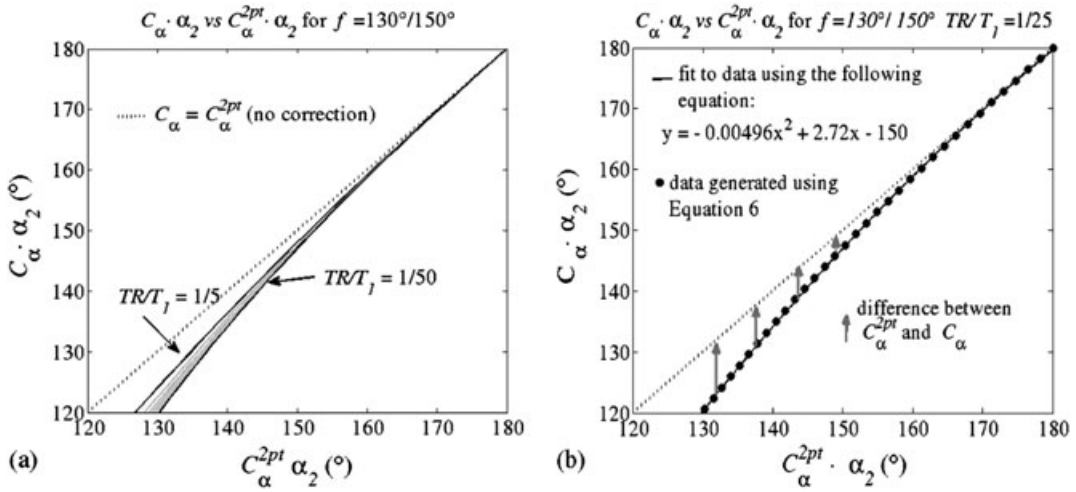

Figure 3. Data is generated using Equation [6] for the indicated values of f and TR/T_1. (a) The curves are generated by evaluating Equation [6] for $f = 130^\circ/150^\circ$ and several values of TR/T_1: $1/50 < TR/T_1 < 1/5$ (grey lines with extremes in black as indicated on graph). It can be seen that the curves do not vary much as a function of TR/T_1. (b) The black dots represent data that is generated by evaluating Eq.[6] for $f = 130^\circ/150^\circ$ and $TR/T_1 = 1/25$ (an average expected value). A fit of this data to the quadratic equation yields an approximate relationship between $C_\alpha^{2pt}\alpha_2$ and $C_\alpha\ \alpha_2$ given by the equation and solid line. The arrows correspond to an *over*estimation of C_α (i.e. *under*estimation of α_{null}) if no correction is used. These arrows are equivalent to those along the horizontal axis in Fig. 3. Once α_2 is chosen for a particular sampling scheme, its value can be replaced in the equation and the relationship between C_α and C_α^{2pt} can be used as a C_α -correction.

NMR IN BIOMEDICINE

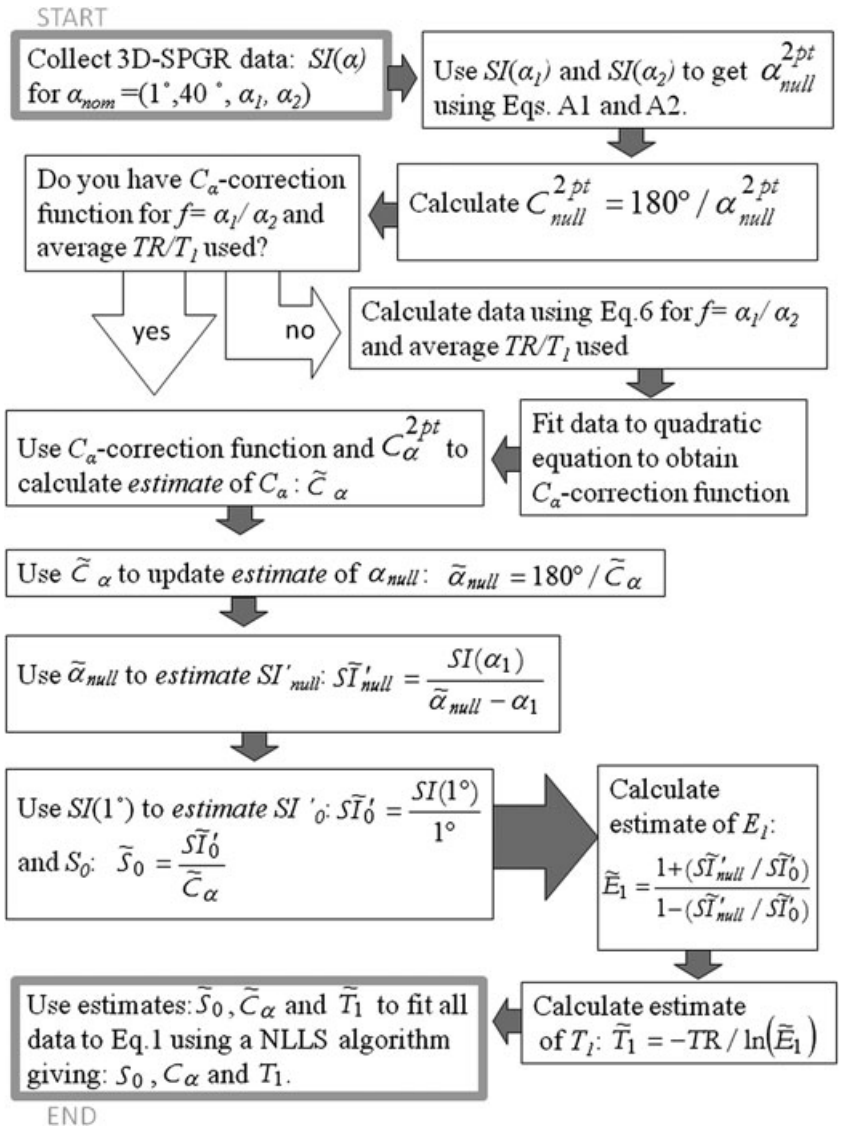

Figure 4. Schematic of steps for MoS. Note that all steps before the NLLS final fitting algorithm (the last box) do not use the *SI*(40°) data point and they do not require any fitting algorithm since straight lines are approximated by two points.

efficiency, by decoupling the sampling for B_1 determination from that for S_0 and T_1.

The α_{nom} = (130°,150°) data points responsible for B_1 estimation are constrained by the linearity condition necessary for accurate extrapolation as described previously. Although extrapolation is expected to be accurate for $TR/T_1 < 1/5$, a constraint on the minimal *TR* exists due to SNR and slope considerations: SNR is reduced and the slope of the curve near the signal null approaches zero as TR/T_1 approaches 0. A conservative rule-of-thumb for *TR* selection was found to be: $TR = T_{1max}/50$, for $T_{1\max} \sim 2000$ ms, this gives $TR = 40$ ms. However, these data points are not constrained to be sampled at high resolution due to the gradual spatial variation of the B_1 map.

Conversely, the α_{nom} =40° data point, responsible for the final T_1 result, should be sampled at high resolution for high resolution T_1 mapping. However, the *TR* time constraint does not apply to it as it is not involved in the straight line extrapolation to signal null. Finally, the α_{nom} =1° data point is expected to be time independent (i.e. independent of TR/T_1) so short TR can be used for both points: α_{nom} = (1°,40°). Although S_0 will have some small-scale spatial variations due to T_2* and proton density variations, for short TE, these are expected to be less intense than the large-scale variations due to coil sensitivities, hence, some spatial resolution can be sacrificed for scan time savings. As long as TE is maintained constant, for the high and low flip angle scans, S_0 is expected to be consistent and thus the ratio of slopes should yield a good estimate of T_1. However, if the TR varies, the final fitting cannot be performed with all the data points. For this reason, only the data at α_{nom} = (1°,40°), with consistent TR, can be used in the fit. However, α_{null}, resulting from the high flip angle data, can be used as a fixed parameter in the final fit which determines S_0 and T_1. To account for varying voxel resolution between the α_{nom} =1° and α_{nom} =40° data, as well as the coarse α_{null} map, all data can be regridded to match the high resolution data, allowing for voxel-wise fitting.

Given these spatial and temporal constraints, the B_1 mapping can be performed for full brain coverage (FOV = 20–22 cm) at coarse resolution (64 × 64 in-plane, 4–5 mm slice thickness) in approximately 4 min. T_1 mapping then requires another fast (short *TR*) volume sampled at α_{nom} =1° and intermediate

resolution (128 × 128 in-plane, 4 mm slice thickness) while a high SNR data point, at α_{nom} =40°, is sampled with high resolution (256 × 256 in-plane, 1 mm slice thickness). Although total scan time depends on head size (i.e. number of slices) and minimal TR available for SPGR, all scans are expected to be performed in <20 min using a standard SPGR sequence (see methods for details).

EXPERIMENTAL METHODS

All experiments were performed on a 3T-MR750 GE scanner (GE, Healthcare) with two GE head coils: a standard quadrature, transmit/receive birdcage coil and a phased-array 8-channel receive-only coil. According to the literature values of T_1 in tissue at 3T (11,12,25,26), the T_1 values considered were: 200 ms–2000 ms. Computations and fitting algorithms were programmed in-house using standard functions in Matlab (The Mathworks Inc., Natick, MA). Simulations and phantom experiments were performed to test the uncertainty and validity of the proposed method respectively. *In vivo* experiments were then performed to demonstrate the ability to yield B_1 and T_1 maps of human brain. All experiments were performed by sampling the signal with the following flip angle sampling scheme: α_{nom} = (1°, 40°, 130°, 150°) based on the aforementioned considerations.

Simulation experiments

Simulations were used to test the error associated with the proposed sampling scheme and C_α-correction scheme. For these simulations, SPGR signal was calculated according to Equation [1] for various known values of S_0, C_α and T_1, at the flip angles of the sampling scheme. The resulting estimates of S_0, C_α and T_1, before and after the NLLS fitting algorithm, were compared to the known values and percent errors (defined as percent difference between estimated and true values) were plotted for TR/T_1 = (1/5, 1/10, 1/15, 1/20, 1/25, 1/30, 1/35, 1/40, 1/45, 1/50). A simple NLLS Levenberg-Marquardt fitting algorithm was used without constraints on the parameter values.

More simulations were run to test the robustness of the proposed MoS under varying levels of SNR. Gaussian distributed noise was added to the SPGR signal generated from Equation [1] representing realistic levels of SNR (this was determined by measuring the signal in regions of a magnitude image of the brain acquired with an 8-channel head coil as proposed by Constantinides *et al*. (29)). The resulting noisy signal at the flip angles given by the proposed sampling scheme was used to determine the initial estimates of S_0, C_α and T_1. A NLLS fitting algorithm was then employed to obtain final estimates for the three parameters. This process was repeated 1000 times to get converging estimates of the average and standard deviation of C_α and T_1, under realistic conditions of SNR. This analysis was used to yield the uncertainty in B_1 and T_1 maps obtained from true data. Several constraints on the possible values of S_0 and C_α were tested to determine the best upper and lower bounds, if any, for robust results.

Phantom experiments

Phantoms consisted of glass beakers containing distilled water doped with varying concentrations of manganese chloride ($MnCl_2$) to obtain varying T_1 values in the range of interest. Two different sizes of beakers were used and will henceforth be referred to as large (base diameter = 10 cm) and small (base diameter = 5 cm).

To test B_1 mapping using the MoS, a large phantom was scanned with the quadrature transmit/receive head coil because this set-up was expected to have large B_1 variations due to the large imaging volume. B_1 inhomogeneities were expected to vary gradually; therefore a coarse time-efficient measurement was sufficient. The use of a large grid also helped increase the SNR for a more robust voxel-wise calculation of B_1. The parameters chosen for this purpose were thus: FOV = 24 cm, 64 × 64 in-plane resolution with a slice thickness = 5 mm. The minimal full echo time (TE = 5 ms) was used in all scans so as to minimize signal loss due to T_2^* effects. For validation, results were compared with B_1 maps obtained from a 2D and a 3D DAM with data sampled at α_{nom} = (60°,120°). For this purpose, the phantom was made to have a short T_1 (~250 ms), so as to allow for the 3D DAM data acquisition in a reasonable time despite the constraint: $TR = 5 \cdot T_1$ (~50 min/data point ~ 1 h 40 min total scan time). TR = 25 ms was used for the MoS although a shorter TR could have been used, based upon $TR = T_{1max}/50$.

To test T_1 mapping using the MoS, several phantoms with differing T_1 values were used. Here, B_1 inhomogeneities were avoided to isolate the factors influencing the T_1 result. Small phantoms were thus used (with small dimensions relative to the expected RF wavelength) placed central to the body coil for transmission with an 8-channel receive-only head coil. For reference, a 2D IR spin echo sequence (IR-SE) was also performed on the phantoms at a single central slice (inversion times: TI = 50,100, 200, 400, 800, 1600, 3200 ms, TR = 5 s). Although time-consuming, IR-SE remains the gold standard method for T_1 mapping. T_1 was calculated voxel-wise by performing a two-parameter, ($p1$, $p2$), NLLS fit of the magnitude data to the longitudinal recovery curve, accounting for imperfect inversion as well as violation of $TR >> T_1$ for larger T_1 values: $S(TI) = p1(1-(1-p2)exp(-TI/T_1) + exp(-TR/T_1))$ (27). A region of interest (ROI) analysis was then used to compare the two results for each phantom.

To test simultaneous B_1/ T_1 mapping using the MoS, a large phantom was scanned with $T_1 \sim 600$ ms, while centered and while shifted to the edge of the quadrature head coil, inducing large B_1 inhomogenities which further challenged the MoS to yield accurate T_1 estimations. The following scan parameters were used: TE/TR = 4 ms/30 ms, 20 cm FOV with 64x64 in-plane resolution, 3 mm slice thickness, 28 coronal slices.

In vivo experiments

In vivo scans were performed on four healthy volunteers (three female, one male, ranging from 25 to 36 years of age) with written consent and in compliance with the ethics board of the institution. For these scans, the 3D slab was placed sagittally such that the entire head was covered in the through-slab direction, allowing for the slab select gradient to be turned off. The scanning parameters were: FOV = 20–24 cm, 128 × 128, slice thickness = 4 mm, 30–40 slices, TE = 5 ms, TR = 40 ms yielding a scan time of approximately 3–4 min per sampled flip angle and total scan time ~16 min. To improve *in vivo* results which, in contrast to phantom experiments, are affected by physiological noise as well as partial volume effects, smoothing was performed on the voxel-wise computed B_1 map. To test the efficient implementation of the MoS, a volunteer was scanned using two protocols: the protocol mentioned above, yielding low

resolution T_1 maps (i.e. 4 mm × 1.72 mm × 1.72 mm), and a modified protocol: $\alpha_{nom} = (130^\circ, 150^\circ)$ acquired with $TE/TR = 5$ ms/40 ms and coarse resolution (~4 min), $\alpha_{nom} = 1^\circ$ acquired with $TE/TR = 6$ ms/18 ms and intermediate resolution (~1 min 40s) and $\alpha_{nom} = 40^\circ$ acquired with $TE/TR = 6$ ms/21 ms and high resolution (~14 min), where coarse, intermediate and high resolution were defined in the previous section. The resulting B_1 and T_1 maps were compared.

Full brain T_1 histograms were obtained by manual extraction of the brain on each slice. The number of voxels was normalized with respect to the maximum peak for better inter-subject comparison, independent of brain size. Peaks were compared with expected T_1 values for grey matter (GM) and white matter (WM). ROI, average and standard deviation T_1 values were also determined and compared with values quoted in the literature (11,12,25,26). Full brain T_1 histograms for coarse and high resolution were compared for the single volunteer scanned with both protocols.

RESULTS

Simulation results

Figure 5 shows the percent error associated with the parameters, S_0, C_α and T_1, determined using the MoS for various values of C_α and T_1 (each curve represents a particular T_1 value). This error depends on the C_α -correction which is sampling-scheme-specific and slightly dependent on the T_1 value used for the fit to the quadratic function (as shown in Fig. 3a). It was found that C_α and S_0 values did not vary significantly after the NLLS fitting and furthermore, the errors associated with the initial estimates were well within acceptable levels (absolute error $< 4\%$ except for the largest value of TR/T_1 and for values $< C_\alpha = 1$). In contrast, the accuracy in determining T_1 was greatly improved using the NLLS fitting algorithm, suggesting that the NLLS fitting is primarily required for T_1 determination under no noise conditions. In all cases, the error was greatest for smaller values of C_α and became insignificant ($<1\%$) as C_α approached and exceeded 1.

Figure 6 shows plots of the resulting $C\alpha$ and T_1 values obtained from simulated noisy signal. For a flip angle of $\alpha_{nom} = 130^\circ$, it was found that SNR > 10 throughout the brain (except in some areas of pure CSF). The smallest SNR values occurred in regions of larger C_α, larger T_1 or smaller S_0. Therefore, σ_{noise} was determined from the SPGR signal corresponding to $\alpha_{nom} = 130^\circ$, $T_1 = 2000$ ms, $C_\alpha = 1.2$ and an SNR = 10. One thousand repetitions ensured convergence of the mean and standard deviation. Constraining the parameters did not significantly improve T_1 accuracy, indicating robustness of this approach. Use of the unconstrained NLLS algorithm resulted in percent errors of average T_1 values reduced to insignificant levels while the uncertainty value was reduced to $<15\%$ as seen by the decrease of standard deviation (Fig. 6). While the NLLS algorithm was less important for the C_α estimate (i.e. initial estimates are accurate to within 5% for most values of C_α and T_1) it was crucial for accurate T_1 results.

Phantom experiments

Profiles of the B_1 maps resulting from the proposed 3D MoS and a 2D and 3D DAM are compared in Fig.7a. It can be seen that the 3D DAM agrees with the 3D MoS to within 3.5% where $C_\alpha > 1$ in the center. Conversely, the 2D DAM result, although qualitatively similar, underestimates C_α significantly (10–20%) in comparison to the MoS such that $C_\alpha < 1$ in the center.

Figure 7b shows the resulting T_1 values for the 3D MoS and for a 2D IR-SE sequence for the small phantoms with varying T_1 values. ROI analysis was performed for a central circle (radius equal to five voxels) within each phantom. Although the dimensions of the phantoms were chosen to reduce B_1 inhomogeneities, it was found that B_1 mapping for MoS was still required, probably as a result of their placement. The results from both methods were plotted against each other. A high correlation was found (Pearson's $r = .997$, $p < 0.0005$) with best fit line, passing through the origin, having a slope of 1.05, indicating good agreement between methods with a slight (5%) overestimation of T_1 values from the MoS relative to the IR-SE.

Figure 8 shows profiles of the 3D B_1 and $T1$ maps resulting from the MoS for a large phantom, scanned while centered and while shifted to the edge of the coil. Profiles of the resulting B_1 and T_1 maps were plotted as a function of position within the coil and compared for the two phantom placements. It can be seen that despite the variations in C_α, the resulting T_1 value is

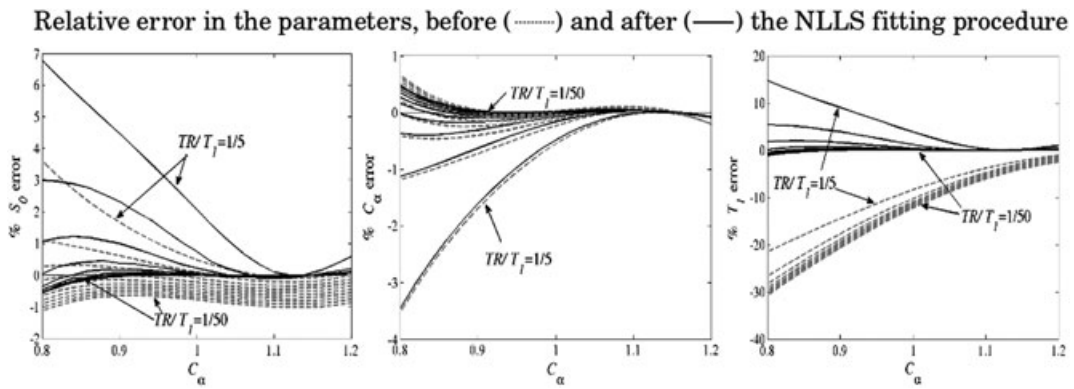

Figure 5. Simulation results comparing errors in the parameters: S_0, C_α and T_1 before and after the NLLS final fitting algorithm. Each curve represents a specific value of TR/T_1. Values plotted are for $TR/T_1 = (1/5, 1/10, 1/15, 1/20, 1/25, 1/30, 1/35, 1/40, 1/45, 1/50)$. The NLLS algorithm is performed without constraints. It can be seen that the NLLS is not required for accurate determination of S_0 and C_α. However, the NLLS fit including the extra data point, $SI(40^\circ)$, is crucial for accurate T_1 estimation, particularly for low values of C_α.

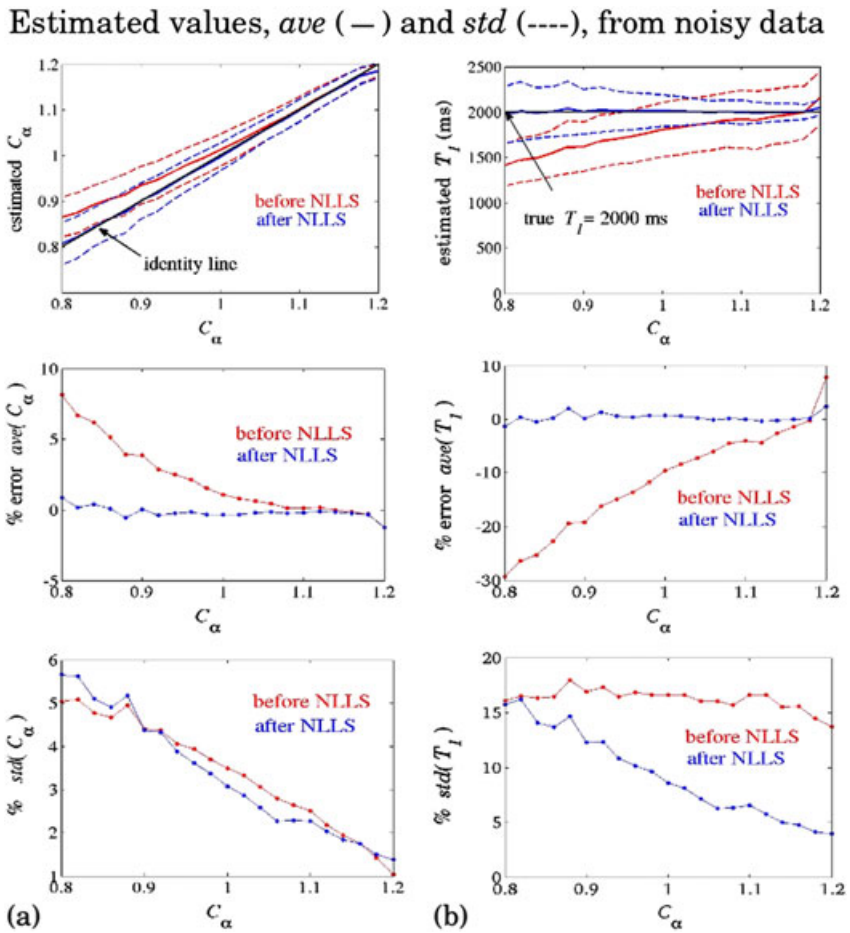

Figure 6. Simulation results testing the robustness of the MoS to noise. Error in the parameters: C_α and T_1 are determined for SNR = 10 at $\alpha_{nom} = 130^\circ$, $T_1 = 2000$ ms and a range of C_α values. Results of the average and standard deviation of C_α and T_1 values are given for 1000 repetitions, before and after all the data is fit by a NLLS algorithm. In this case, it was found that constraining the NLLS was not necessary to achieve accurate C_α and T_1 results (seen by the % error of average ~0% for all C_α values, second row).

constant as expected for this homogeneous phantom (with the exception of a small region, near the edge of the coil, where the RF cannot penetrate (shaded in Fig. 8c)).

In vivo experiments

Figure 9 shows central slices of the 3D B_1 and T_1 maps resulting from *in vivo* measurements on one of the volunteers using the proposed MoS with both low resolution (a) and high resolution (b) protocols. The techniques used to produce reference B_1 and T_1 maps for the phantoms are prohibitively too long to be used *in vivo*. Results are hence compared with expected B_1 maps and T_1 values from the literature.

Full brain T_1 histograms for the volunteers are shown in Fig. 10a. The values corresponding to WM and GM occur at two peaks which coincide at approximately 1100 ms and 1700 ms, respectively. These values are in agreement with T_1 values given in the literature: WM ~ 950–1080 ms, GM ~ 1550–1820 ms (11,12,25,26). Also, ROI analysis, performed in representative regions for GM and WM on all subjects gave average and standard deviation T_1 values which are presented in Table 1. A comparison of full brain T_1 histograms for a single volunteer at high and low resolution is shown in Fig.10b.

DISCUSSION

The goal of the proposed method was to produce simultaneous B_1 and T_1 maps efficiently, with readily available sequences and simple fitting algorithms. The C_α -correction scheme is an essential component of the efficiency of the proposed method because it allows for accurate estimation of C_α, for a large range of C_α and T_1 values, by a simple 2 pt-extrapolation. We have shown that even if we choose $TR/T_1 = 40/1000$ for the fit to derive the C_α -correction scheme, most other T_1 values of interest are also well corrected (<5% error, Fig. 5). The larger error (>5%) occurring for $TR/T_1 = 1/5$ and small C_α values could be reduced by using a better C_α -correction scheme, obtained by simply choosing a smaller T_1 value to fit the C_α -correction curve. This post-processing step would not interfere with the required scanning. In fact, the C_α -correction scheme can be slightly adjusted depending on the sought accuracy associated with the various C_α and T_1 values of the application. Given that the T_1 dependency of the C_α -correction curves increases as C_α decreases (Fig. 3a), a single C_α -correction scheme may not be adequate if a very large range of T_1 and C_α values are observed, particularly for smaller C_α values (<0.8). In such a case, one could apply two or more C_α -correction schemes derived from curves

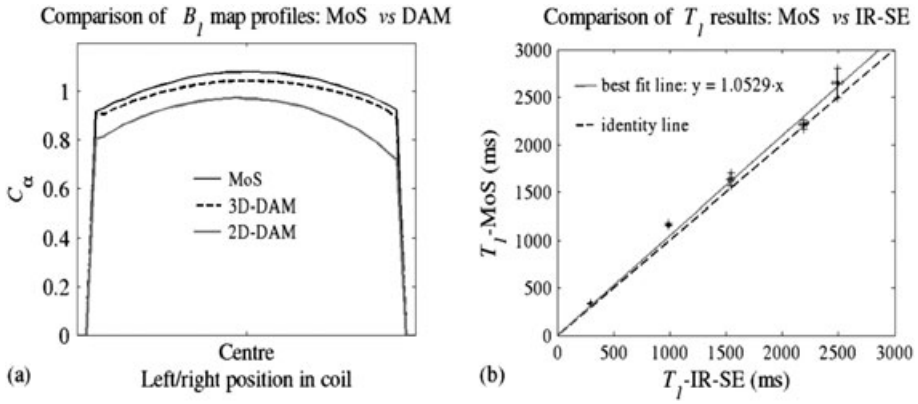

Figure 7. Comparison of B_1 and T_1 mapping results using the MoS and other well-established standard techniques. (a) Profiles of the resulting B_1 maps along the center of a large phantom are compared for the 3D-MoS and 2D- and 3D-DAM. The 3D-MoS matches the 3D-DAM quite closely while the 2D-DAM relatively underestimates the B_1 values. (b) Results of the ROI analyses of the T_1 maps of five small phantoms are compared. Resulting average standard deviation T_1 values are plotted for MoS against the IR-SE experiment. Pearson's correlation coefficient, r = .997 ($p < .005$), with the line fit having slope = 1.05 as shown.

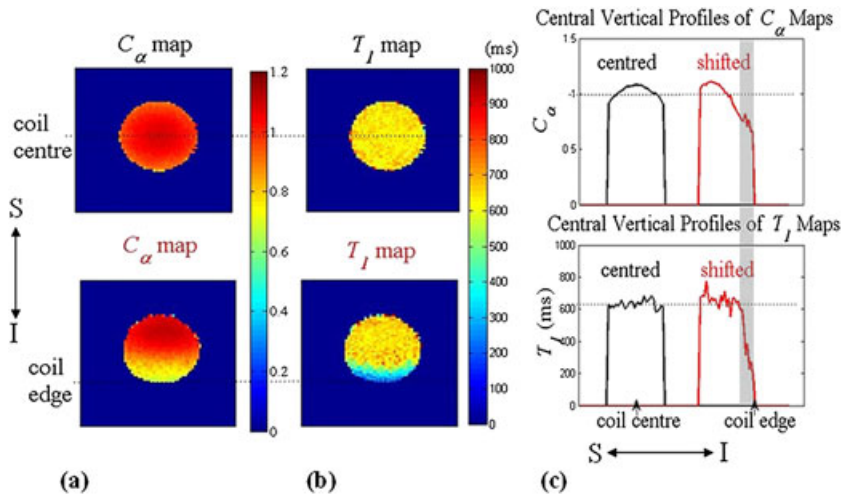

Figure 8. Results using the MoS on a large phantom while well-centered in the quadrature transmit/receive head coil and while shifted in the superior-to-inferior direction (S→I) to the inferior edge of the coil. Columns (a) and (b) show the C_α and T_1 maps of a central slice respectively, for both phantom placements (top row = centered phantom, bottom row = shifted phantom). The central vertical (S/I) profiles of the maps shown in (a) and (b) are plotted for both phantom placements in (c) (the centered phantom profiles are shown in black and the shifted phantom profiles are shown in red). Note the S/I orientation is rotated in (c) with respect to (a) and (b). The shaded area shows the region within the coil where the B_1 field is not able to produce high flip angles adequately, i.e. in this region, the linear relation between α_{nom} and α is no longer valid for high flip angle values. This region lies close to the edge of the coil.

generated for two or more T_1 values and then select the T_1 result appropriately. For the purposes of brain imaging with a head coil, this is not necessary since $C_\alpha > 0.8$ is expected.

The results for the noise simulation tests, presented in Fig. 6, indicate that B_1 mapping by the MoS is very robust. In fact, the 2 pt-extrapolation with C_α -correction scheme alone is capable of estimating the B_1 map to within 8% error, where the maximum error results at small C_α for $T_1 = 2000$ ms, due to low SNR and long-range extrapolation. The NLLS algorithm further improves this B_1 map. However, the T_1 values derived from a simple ratio of slopes (initial estimates) are very sensitive to low SNR due to the non-linear relationship between the slope values and resulting T_1, given by Equation [5] (Fig. 6b). The robustness of the NLLS fitting algorithm (Fig. 6b) can be attributed to two factors: (i) the accuracy of the initial estimates of S_0 and C_α, based on the data at $\alpha_{nom} = (1^\circ, 130^\circ, 150^\circ)$; and (ii) the inclusion of the high SNR data point in a region of high T_1-dependence of the signal: $\alpha_{nom} = 40^\circ$. In fact, solving explicitly for S_0 and C_α, before solving for T_1, and constraining S_0 and C_α to vary very little (<1%) during the NLLS fit to the $\alpha_{nom} = 40^\circ$ data point, results in accurate T_1 results regardless of the initial T_1 estimate (data not shown).

Phantom experiments validated the B_1 and T_1 mapping capability of the proposed method (Fig. 7). The 3D-SPGR DAM agrees closely with the B_1 map resulting from the proposed 3D MoS. Although the 2D-DAM results in a qualitatively similar B_1

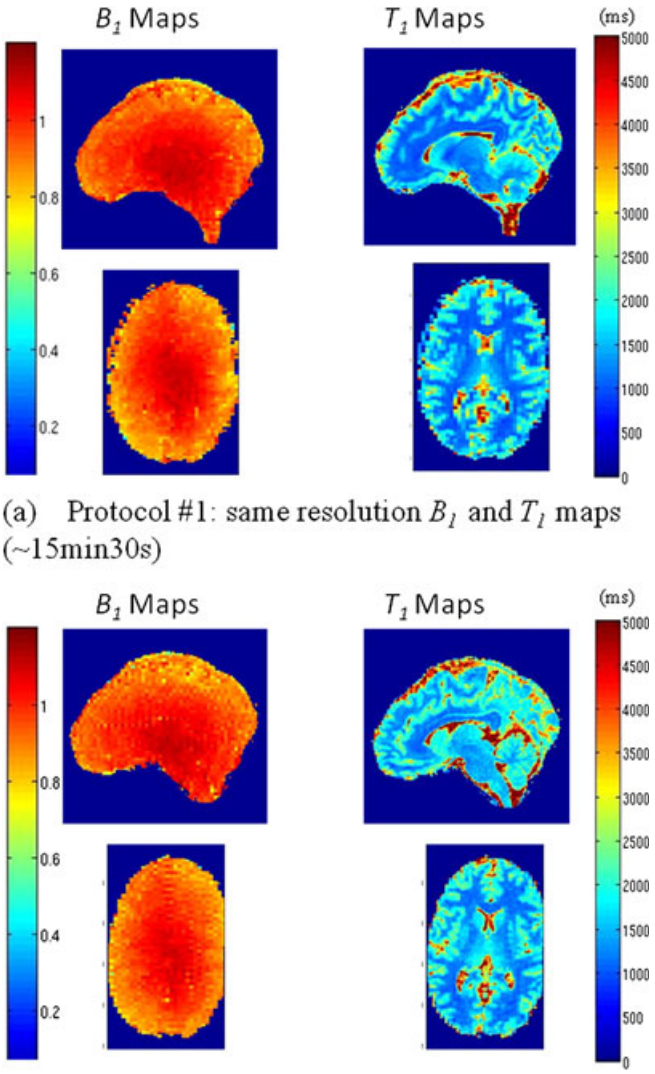

Figure 9. Representative *in vivo* B_1 and T_1 mapping: shown is the central slice of a 3D full brain scan for one of the volunteers. Scans were performed sagitally and reconstructed axially. (a) Representative B_1 and T_1 maps using the MoS as initially proposed, giving a resolution of 128×128 with a slice thickness = 4 mm for both B_1 and T_1 maps. (b) Representative B_1 and T_1 maps resulting using the MoS with the more efficient protocol proposed, yielding a coarser resolution B_1 map (64×64, slice = 4 mm) and a higher resolution T_1 map (256×256, slice = 1 mm).

map profile as that for the 3D-, the absolute values were *under*estimated by a considerable amount (10–20%). This is most likely due to slice profile considerations (28) which would result in an overestimation of the signal at $\alpha_{nom} = 120^\circ$. This result indicates that although the use of a 2D-DAM B_1 map correction to flip angle values prior to T_1 mapping may 'flatten' the result in a desirable way, the absolute value of the T_1 map may still be erroneous, emphasizing the benefit of using a simultaneous 3D- B_1 and T_1 mapping method such as the MoS.

The IR-SE experiment was performed on several small phantoms with varying T_1 values (~250–2500 ms). MoS was also performed with $TR = 30$ ms, resulting in values of $TR/T_1 \sim 1/8 - 1/80$ since all phantoms were placed simultaneously in the coil for this experiment. The scan time was ~2 min per data point and hence B_1 and T_1 values were obtained in a total of ~8 min of scan time. An ROI analysis indicated that IR-SE and MoS T_1 values are in agreement, with a slight T_1 overestimation (5%) from the MoS relative to the IR-SE results. Also, the MoS becomes more unreliable (i.e. larger standard deviation) for T_1 values greater than 2000 ms (Fig. 7b). A T_1 overestimation for the VFA relative to the IR method has previously been observed (4) and it has been shown to result from noisy data. Noise and artifacts, both increasing low SNR signal from its expected value, may be the source of overestimation for these phantom experiments as well, but this requires further investigation. Artifacts, such as Gibbs ringing, susceptibility induced distortions, and improper spoiling, were evident in the small phantom data. Improper spoiling has been noted as a main source of error in the AFI method of Yarnykh (30) due to the short *TR*s that were initially proposed. It has also been studied as a main source of error in the VFA methods which also rely on the SPGR signal at very short *TR* (31). In our case, the MoS does not require such short *TR* and spoiling artifacts have not been noticed *in vivo*. However, inadequate spoiling could have been a source of error in phantom experiments due to their longer T_2 values. All artifacts were less significant for the phantoms with smaller T_1 due to their higher SNR. Given the T_1 values of the phantoms, a larger *TR*, could have been used to improve SNR at the expense of some scanning efficiency. A general suggestion based on the SPGR vs α_{nom} curves is that TR/T_1 should be kept $\geq 1/50$ which is reinforced by these results as the IR-SE and MoS T_1 values are in very good agreement and have smaller standard deviations for T_1 values $\leq$1500 ms (i.e. the first three data points). This effect is not expected to be such an issue *in vivo* where shorter T_2 values and fewer edge-induced artifacts are expected.

Scanning the large phantom in two positions within the coil, demonstrated that in the presence of large B_1 variations, the resulting T_1 value can be determined accurately. The average T_1 value of the well-centered phantom was 637 ms with a standard deviation of 25 ms whilst the T_1 value of the shifted phantom was 650 ms with a standard deviation of 39 ms. The difference in the averages was only 2% despite the large B_1 variations (Fig. 8). The MoS was successful until a few centimeters near the edge of the coil where the B_1 transmit field was no longer able to produce large flip angles. In this region (shaded in Fig. 8c), the assumed linear relationship between α and α_{nom} no longer holds for large α_{nom} values (i.e. as α_{nom} increased, the signal did not change significantly). Scanning in this region is avoided in practice because the coil is not expected to produce an effective B_1 field so close to the edge.

In vivo experiments demonstrated that the MoS is capable of yielding brain B_1 and T_1 maps in a reasonable scan time for all subjects (<18 min). As mentioned previously, there is no theoretical *TR* restriction for the T_1 mapping data, $\alpha_{nom} = (1^\circ, 40^\circ)$, hence a fast SPGR (FSPGR) sequence could be used to minimize the *TR* and hence scan time. This was not attempted in this study to eliminate confounding sources of inaccuracy but it will be further investigated and scan times comparable to the VFA method are expected.

ROI analysis and full-brain histograms of T_1 results give confidence in the results as the values obtained compare well with those in the literature (11,12,25,26). The large range of values (and associated standard deviations) for GM presented in Table 1, as well as in the literature, probably arises due to partial volume

NMR IN BIOMEDICINE

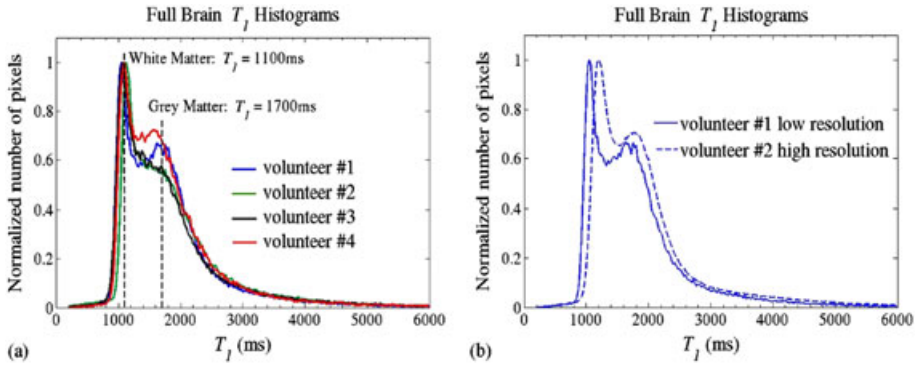

Figure 10. Overlayed histograms of full brain data. (a) comparison for all volunteers (b) comparison for the same volunteer, with different protocols. There appear to be 2 peaks which coincide for all volunteers, one corresponding to the mean value of T_1 for white matter (WM) and the other for grey matter (GM): WM- T_1 =1100 ms and GM- T_1 =1700 ms. These values are in agreement with values quoted in the literature: WM ~ 900–1080 ms, GM ~ 1350–1820 ms (11,12,23,24)).

Table 1. Table of T_1 values in representative ROIs for GM and WM

Volunteer #	T_1 of GM (*ms*)		T_1 of WM (*ms*)	
	ROI-1	ROI-2	ROI-1	ROI-2
1	1586 ± 544^b	1558 ± 483^b	1216 ± 205^b	1073 ± 150^b
	1496 ± 172^a	1523 ± 72^a	1031 ± 69^a	988 ± 55^a
2	1522 ± 146^a	1586 ± 63^a	1074 ± 51^a	1058 ± 50^a
3	1752 ± 186^a	1599 ± 87^a	1135 ± 88^a	968 ± 72^a
4	1622 ± 190^a	1531 ± 101^a	1013 ± 116^a	1030 ± 78^a

[a]Values indicate the average ± std within ROIs consisting of a small region of approximately 25 voxels placed on a single sagittal slice in representative regions of WM = white matter (1-splenium, 2- genu of corpus callosum) and GM = grey matter (1-frontal cortex, 2-thalamus).
[b]High resolution protocol #2 (on volunteer #1 only). ROI consists of approximately 100 voxels placed on 4 sagittal slices in same regions as a.

effects since gray matter is in close proximity to WM and CSF with low and high T_1 values, respectively. This is also evident in the large width of the GM peak in the full-brain histograms (Fig.10a) and a possible reason for the slight overestimation of T_1 values at higher resolution. In large voxels, containing tissues with low and high T_1 values, the tissues with low T_1 values will dominate the signal (due to the inverse relation of T_1 in E_1) yielding an average T_1 value:

$1/(T_1)_{ave} = \frac{1}{2}(1/(T_1)_{low} + 1/(T_1)_{high})$. Resolution may therefore also be an important source of variation in T_1 values reported in the literature, although the contribution from increased noise in the high resolution scans must also be considered.

Although the MoS uses relatively large flip angles (130°, 150°), these are close in value to the high flip angle commonly used for a DAM: (60°, 120°). The potentially damaging specific absorption rate (SAR) associated with these scans was found to be well within standard scanner limits and far less a factor than for other SAR-intense sequences with inversion pulses. This is probably due to the fact that the SAR limit for human scanning is given as a time-average maximum, the short scans (~3 min) at the high flip angle values as well as scanning in the following order: (1°, 130°, 40°, 150°) resulted in time-averages that did not exceed 20% of the limit (as indicated on the scanner), for all scans conducted *in vivo*. SAR is thus not a concern for these scans.

The most restrictive limitation of the proposed technique lies in the fact that it requires 3D sampling for quantitative accuracy. This is not so much a limitation for the B_1 mapping portion due to the low resolution required: a full brain B_1 map can be obtained in approximately 3–4 min which is comparable with the AFI method. However, it greatly limits the minimal scan time for high resolution T_1 mapping. Although this is a limitation it shares with the other popular VFA technique, a 2D T_1 mapping technique is highly desirable. Using the MoS approach, a single-slice T_1 map could be acquired in a very short time from a single sample at $\alpha = 40°$ (assuming B_1 and S_0 have been determined from quick, low-resolution 3D scans at $\alpha = 1°$ and $\alpha = (130°, 150°)$ respectively). This would be ideal for dynamic contrast enhanced, DCE, MRI where temporal resolution is important. The 3D requirement is a difficult limitation to overcome if the optimal sampling scheme is dependent on the expected T_1 value of interest as is the case for the VFA method (10). However, the proposed scheme is not T_1 -dependent. The MoS T_1 mapping ultimately relies on the single sample at $\alpha = 40°$, for any T_1 value. This is an important distinction between the VFA method and the MoS since the use of a fixed sampling scheme may facilitate overcoming the 3D restriction. A flip angle dependent RF waveform, such as an SLR pulse, could provide ideal 2D slice profiles for the desired flip angle, $\alpha = 40°$.

CONCLUSIONS

The MoS samples the SPGR signal at high flip angles and uses an extrapolation to signal null for B_1 mapping as in Ref. 21. However, it improves upon the original signal null method in that fewer and smaller flip angles can be used due to the C_α-correction scheme introduced. The MoS then samples the SPGR signal at low flip angles, $\alpha_{nom} = (1^\circ, 40^\circ)$, similar to the VFA method ($\alpha_{nom} = (2^\circ, 9^\circ, 19^\circ)$ for $TR = 5$ ms, (11)). However, the MoS uses the full SPGR signal equation, and characteristics of the signal *vs* flip angle curves, to solve for T_1. This is in contrast to the VFA method which uses a linear form of the equation which has a singularity, is known to introduce a noise bias and requires a minimum of three sampled points for possible use of a weighted least-squares fit (11). The result of this work is a novel, accurate and consistent simultaneous B_1 and T_1 mapping method.

The method presented here is proposed for brain imaging, but it could easily be applied in other relatively stationary anatomical regions and for other coils. For the B_1 mapping portion, the maximal flip angle sampled must occur before the signal is nulled throughout the FOV and scan time can be minimized using the rule-of-thumb: TR $= T_{1max}/50$. For the T_1 mapping portion of the MoS, $\alpha_{nom} = (1^\circ, 40^\circ)$ can be used regardless of the T_1 of interest and minimal TR is determined by the ability of the scanner to achieve proper spoiling of the SPGR signal. The MoS currently requires 3D data acquired without the slab select gradient for accuracy. This will result in scan times in the order of minutes per data point which precludes breath-holding techniques as well as dynamic studies. Full brain coverage at 0.8 mm × 0.8 mm × 1 mm resolution was possible in <18 min scan time (dependent only on head size) but could possibly be improved by the use of shorter TR values (using a fast SPGR sequence). Investigation into a 2D MoS is also currently underway.

Acknowledgements

The authors would like to thank Rafal Janik for his insightful discussions about RF inhomogeneities as well as the Canadian Institutes of Health Research, CIHR, for its funding support.

REFERENCES

1. Gambarota G, Veltien A, van Laarhoven H, Philippens M, Jonker A, Mook OR, Frederiks WM, Heerschap A. Measurements of T-1 and T-2 relaxation times of colon cancer metastases in rat liver at 7T. Magn. Reson. Mater. Phys. 2004; 17(3–6): 281–287.
2. Bailey C, Giles A, Czarnota GJ, Stanisz GJ. Detection of Apoptotic Cell Death In Vitro in the Presence of Gd-DTPA-BMA. Magn. Reson. Med. 2009; 62(1): 46–55.
3. Vaithianathar L, Tench CR, Morgan PS, Constantinescu CS. Magnetic resonance imaging of the cervical spinal cord in multiple sclerosis – A quantitative T-1 relaxation time mapping approach. J. Neurol. 2003; 250(3): 307–315.
4. Vavasour IM, Li DKB, Laule C, Traboulsee AL, Moore GRW, MacKay AL. Multi-parametric MR assessment of T-1 black holes in multiple sclerosis. J. Neurol. 2007; 254(12): 1653–1659.
5. Sampson C, Edmondson R, Keegan J, Humphreys S, Hughes R, Talbot D, Andrews P, Firmin D, Longmore D. MR high-resolution imaging of arterial intimal hyperplasia at 1.5T. Magn. Reson. Mater. Phys. 1994; 2(3): 315–318.
6. Look DC, Locker DR. Time saving in measurement of NMR and EPR relaxation times. Rev. Sci. Instrum. 1970; 41: 250–251.
7. Gowland P, Mansfield P. Accurate measurement of T1 in-vivo in less than 3 seconds using echo-planar imaging. Magn. Reson. Med. 1993; 30(3): 351–354.
8. Ordidge RJ, Gibbs P, Chapman B, Stehling MK, Mansfield P. High-speed multislice T1 mapping using inversion-recovery echo-planar imaging. Magn. Reson. Med. 1990; 16(2): 238–245.
9. Wang HZ, Riederer SJ, Lee JN. Optimizing the precision in T1 relaxation estimation using limited flip angles. Magn. Reson. Med. 1987; 5(5): 399–416.
10. Deoni SCL, Rutt BK, Peters TM. Rapid combined T-1 and T-2 mapping using gradient recalled acquisition in the steady state. Magn. Reson. Med. 2003; 49(3): 515–526.
11. Cheng HLM, Wright GA. Rapid high-resolution T-1 mapping by variable flip angles: Accurate and precise measurements in the presence of radiofrequency field inhomogeneity. Magn. Reson. Med. 2006; 55(3): 566–574.
12. Wang JH, Qiu ML, Kim H, Constable RT. T-1 measurements incorporating flip angle calibration and correction in vivo. J. Magn. Reson. 2006; 182(2): 283–292.
13. Barral JK, Gudmundson E, Stikov N, Etezadi-Amoli M, Stoica P, Nishimura DG. A robust methodology for in vivo T_1 mapping. Magn. Reson. Med. 2010; 64(4): 1057–1067.
14. Weiskopf M., Lutti A., Helms G., Novak M., Ashburner J., Hutton C. Unified segmentation based correction of R1 brain maps for RF transmit field inhomogeneities (UNICORT). Neuroimage 2011; 54: 2116–2124.
15. Dietrich O, Reiser MF, Schoenberg SO. Artifacts in 3-T MRI: Physical background and reduction strategies. Eur. J. Radiol. 2008; 65(1): 29–35.
16. Stollberger R, Wach P. Imaging of the active B-1 field in vivo. Magn. Reson. Med. 1996; 35(2): 246–251.
17. Cunningham CH, Pauly JM, Nayak KS. Saturated double-angle method for rapid B-1 plus mapping. Magn. Reson. Med. 2006; 55(6): 1326–1333.
18. Morrell GR. A phase-sensitive method of flip angle mapping. Magn. Reson. Med. 2008; 60(4): 889–894.
19. Yarnykh VL. Actual flip-angle imaging in the pulsed steady state: A method for rapid three-dimensional mapping of the transmitted radiofrequency field. Magn. Reson. Med. 2007; 57(1): 192–200.
20. Sacolick L, Wiesinger F, Hancu I, Vogel M. B1 mapping by Bloch-Siegert shift. Magn. Reson. Med. 2010; 63(5): 1315–1322.
21. Dowell NG, Tofts PS. Fast, accurate, and precise mapping of the RF field in vivo using the 180 degrees signal null. Magn. Reson. Med. 2007; 58(3): 622–630.
22. Tardif CL, Stikov N, Levesque I, Pike BG. Impact of three B1 mapping techniques on variable flip angle T1 measurements. *Proceedings of the 19th International Society on Magnetic Resonance in Medicine (ISMRM)*, 2011; 2745.
23. Venkatesan R, Lin W, Haacke M. Accurate determination of spin-density and T_1 in the presence of RF-field inhomogeneities and flip-angle miscalibration. Magn. Reson. Med. 1998; 40(4): 592–602.
24. Deoni SCL. High-resolution T1 mapping of the brain at 3T with driven equilibrium single pulse observation of T1 with high-speed incorporation of RF field inhomogeneities (DESPOT1-HIFI). J. Magn. Reson. Imaging 2007; 26(4): 1106–1111.
25. Fleysher R, Fleysher L, Liu S, Gonen O. TriTone: a radiofrequency field (B_1)-insensitive T1 estimator for MRI at high magnetic fields. Magn. Reson. Med. 2008; 26(6): 781–789.
26. Stanisz GJ, Odrobina EE, Pun J, Escaravage M, Graham SJ, Bronskill MJ, Henkelman RM. T-1, T-2 relaxation and magnetization transfer in tissue at 3T. Magn. Reson. Med. 2005; 54(3): 507–512.
27. Gupta RK, Ferretti JA, Becker ED, Weiss GH. A modified fast inversion-recovery technique for spin–lattice relaxation measurements. J. Magn. Reson. 1980; 38: 447–452.
28. Parker GJM, Barker GJ, Tofts PS. Accurate multislice gradient echo T-1 measurement in the presence of non-ideal RF pulse shape and RF field nonuniformity. Magn. Reson. Med. 2001; 45(5): 838–845.
29. Constantinides CD, Atalar E, McVeigh ER. Signal to noise measurements in magnitude images from NMR phased arrays – (Vol. 38, p. 852, 1997). Magn. Reson. Med. 2004; 52(1): 219–219.
30. Yarnykh VL. Optimal radiofrequency and gradient spoiling for improved accuracy of t-1 and b-1 measurements using fast steady-state techniques. Magn. Reson. Med. 2010; 63:1610–1626.
31. Preibisch C, Deichmann R. Influence of RF spoiling on the stability and accuracy of T1 mapping based on spoiled FLASH with varying flip angles. Magn. Reson. Med. 2009; 61: 125–135.

NMR IN BIOMEDICINE

APPENDIX

A two-point (2 pt) straight line extrapolation to signal null yields an estimate of the flip angle for signal null: α_{null}^{2pt}. An expression for α_{null}^{2pt} can be written as a function of the sampled signal intensity, *SI*, at each of two flip angles, α_1 and α_2 (Fig. 3): $SI_1 = SI(\alpha_1)$ and $SI_2 = SI(\alpha_2)$ as follows:

$$\alpha_{null}^{2pt} = -\frac{SI_1}{m} + \alpha_1 \tag{A1}$$

where m is the slope defined by the two data points: SI_1 and SI_2, given by:

$$m = -\frac{(SI_1 - SI_2)}{(\alpha_2 - \alpha_1)} \tag{A2}$$

Using Equation [A2] in Equation [A1] gives:

$$\alpha_{null}^{2pt} = \frac{\alpha_2 SI_1 - \alpha_1 SI_2}{SI_1 - SI_2} \tag{A3}$$

Writing $\alpha_1 = f \cdot \alpha_2$, where f is a fraction <1 by definition (since $\alpha_1 < \alpha_2$), Equation [A3] can be rewritten:

$$\frac{\alpha_{null}^{2pt}}{\alpha_2} = \frac{SI_1 - f \cdot SI_2}{SI_1 - SI_2} \tag{A4}$$

Using Equation [1] to write SI_i as a function of: E_1, S_0 and $\alpha_{i\ true}$ where $\alpha_{i\ true} = C_\alpha \cdot \alpha_i$, Equation [A4] becomes:

$$\frac{\alpha_{null}^{2pt}}{\alpha_2} = \frac{A(C_\alpha \cdot f \cdot \alpha_2) \cdot B(C_\alpha \cdot \alpha_2) - f \cdot A(C_\alpha \cdot \alpha_2) \cdot B(C_\alpha \cdot f \cdot \alpha_2)}{A(C_\alpha \cdot f \cdot \alpha_2) \cdot B(C_\alpha \cdot \alpha_2) - A(C_\alpha \cdot \alpha_2) \cdot B(C_\alpha \cdot f \cdot \alpha_2)} \tag{A5}$$

where A and B are defined for an arbitrary angle, ϕ, as:

$A(\phi) = sin(\phi)$ and $B(\phi) = (1 - E_1 cos(\phi))$ to simplify the notation. Noting that $C_\alpha = 180^\circ/\alpha_{null}$, Equation [A5] describes the relationship between the estimated, α_{null}^{2pt}, and true, α_{null}, it can be used to determine a plot of α_{null}/α_2 *vs* $\alpha_{null}^{2pt}/\alpha_2$. If α_2 is chosen to be equal to the smallest expected α_{null} value, relevant values of α_{null}/α_2 will be from 1 to 1.5. Using these values in Equation [A5] to compute $\alpha_{null}^{2pt}/\alpha_2$ for several values of f and relevant values of E_1 yields the curves shown in Fig. A1. The value of f is color-coded while the various values of E_1 (corresponding to a five-fold variation in TR/T_1 i.e. from 1/10 to 1/50) are shown by the small spread of alike-colored lines. The curves demonstrate that, as α_{null}^{2pt} moves away from α_2, α_{null} is gradually more underestimated (as demonstrated in Fig. 3 as well). This relationship follows a smooth curve that is not very dependent on the exact value of E_1 (small spread of like-colored lines). Determination of such a curve *a priori* could be used to predict α_{null} given α_{null}^{2pt} and the fact that all other factors are known scanning parameters: α_2, $f = \alpha_1/\alpha_2$ and an estimate of E_1 (determined by the choice of *TR* and an average of expected T_1 values).

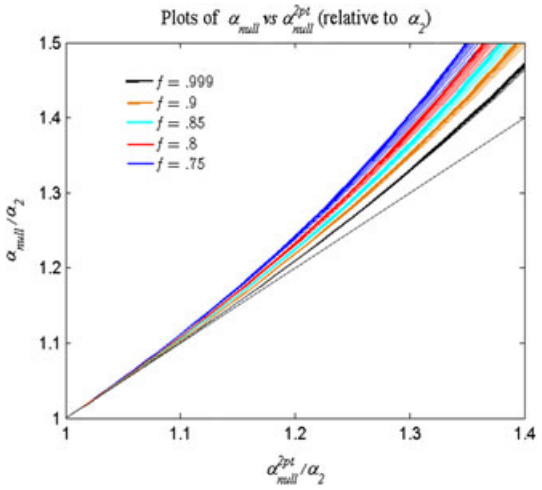

Figure A1. Plot of α_{null}/α_2 vs $\alpha_{null}^{2pt}/\alpha_2$ for various values of $f = .75$–$.999$ (color-coded) and E_1 (spread of like-colored lines) for TR/ T_1 =1/50–1/5. Some curves with TR/ T_1 <1/25 have been omitted for clarity as the curves overlap slightly between the different colors for the smaller TR/ T_1 values, in particular for the smaller f values. Note that $f = \alpha_1/\alpha_2$ is determined by the choice of sampling flip angles so the only approximated value required to generate the curve is E_1. As shown, a five-fold change in TR/ T_1 does not cause a significant change in any of the curves (moreover, a 10-fold change in TR/ T_1 does not cause a significant change in the curves for higher f values $> .85$).

